


# 1 Structural Coloring of Glass Using Dewetted Nanoparticles and 2 Ultrathin Films of Metals

3 Renwen Yu,<sup>†</sup> Prantik Mazumder,<sup>‡</sup> Nick F. Borrelli,<sup>‡</sup> Albert Carrilero,<sup>†</sup> Dhriti S. Ghosh,<sup>†</sup>  
4 Rinu A. Maniyara,<sup>†</sup> David Baker,<sup>‡</sup> F. Javier García de Abajo,<sup>\*,†,§</sup> and Valerio Pruneri<sup>\*,†,§</sup>

5 <sup>†</sup>ICFO-Institut de Ciències Fòniques, The Barcelona Institute of Science and Technology, 08860 Castelldefels (Barcelona), Spain

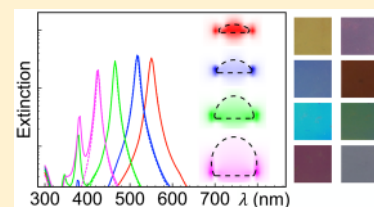
6 <sup>‡</sup>Corning Inc., Sullivan Park, Corning, New York 14830, United States

7 <sup>§</sup>ICREA-Institució Catalana de Recerca i Estudis Avançats, Passeig Lluís Companys 23, 08010 Barcelona, Spain

8  Supporting Information

9 **ABSTRACT:** Metal nanoparticles have been used for coloring glass since antiquity.  
10 Colors are produced by light scattering and absorption associated with plasmon  
11 resonances of the particles. Recently, dewetting at high temperature has been  
12 demonstrated as a straightforward high-yield/low-cost technique for nanopatterning  
13 thin metal films into planar arrays of spherical nanocaps. Here, we show that by simply  
14 tuning the contact angle of the metal dewetted nanocaps one can achieve narrow  
15 resonances and large tunability compared with traditional approaches such as changing  
16 particle size. A vast range of colors is obtained, covering the whole visible spectrum and  
17 readily controlled by the choice of film thickness and materials. The small size of the particles results in a mild dependence on  
18 incidence illumination angle, whereas their high anisotropy gives rise to strong dichroism. We also show color tuning through  
19 interference by simply adding an ultrathin metal film at a designated distance from the dewetted particle array. Our  
20 measurements are quantitatively well explained through analytical theory, which enables fast optimization of fabrication  
21 parameters. Good agreement between theory and experiment requires incorporating the effect of plasmon peak broadening  
22 caused by the finite size distribution of the particle. The proposed designs and techniques hold great potential for large-scale  
23 production of colored and dichroic glass with application to optical windows, filters, and displays.

24 **KEYWORDS:** structural colors, dewetting, plasmonics, glass coloring



25 **E**arly evidence of dichroic colored glass can be found as  
26 soon as fourth century Rome: the celebrated Lycurgus  
27 Cup,<sup>1</sup> whose color changes between red and green depending  
28 on the illumination angle. We had to wait until recent times to  
29 understand that coloring was produced by dispersed silver  
30 nanoparticles, whose localized surface plasmon resonances  
31 (LSPRs) affect very differently the light spectra in either  
32 reflection or transmission. Based on this effect and on the  
33 dependence of LSPRs on particle size, shape, and composition,  
34 various strategies have been explored for structural color-  
35 ing,<sup>2–12</sup> including LSPR hybridization in metal nanodisks and  
36 nanoholes.<sup>13</sup>

37 Modern dichroic colored glass is however based on thin-film  
38 interference, which is widely used in a variety of commercial  
39 optical filters<sup>14</sup> to produce narrow spectral bands for  
40 applications such as fluorescence microscopy<sup>15</sup> and LCD  
41 projectors.<sup>16</sup> On the exploratory side, intense research efforts  
42 are being devoted to creating bright structural colors through  
43 thin-film interference involving ultrathin metal films  
44 (UTMFs)<sup>17</sup> and lossy dielectric layers on top of metals.<sup>18</sup>

45 In many applications it is crucial to create colors in a  
46 transparent substrate (e.g., glass) via surface nanostructuring.<sup>19</sup>  
47 This is a flexible strategy that can be applied to virtually any  
48 glass and does not require bulk modifications, such as the  
49 addition of inclusions. However, in order to attract industrial

interest, it must be low cost and mass scalable. Intensive optical  
50 and electron-beam nanolithography are therefore not an  
51 option. Instead, dewetting of UTMFs has recently been  
52 shown to provide an efficient way of forming metal nano-  
53 particles on large silica surfaces.<sup>20–22</sup> The process consists in  
54 depositing a continuous UTMF and heating it to several  
55 hundred degrees Celsius, so that the film contiguity disappears  
56 and the metal groups together into nanoparticles with  
57 characteristic size distributions. Surface energies of UTMF  
58 and substrate as well as the interfacial energy between them  
59 drive the particle shape into nanocaps of well-determined  
60 contact angle  $\beta$  with the substrate.<sup>23</sup> Interestingly, the particle  
61 size and surface density can be controlled by the original film  
62 thickness, as well as by the duration and temperature of the  
63 heating treatment.<sup>24</sup> Metal dewetting is thus a viable option for  
64 simple, low-cost lithography-free surface nanostructuring,  
65 which is ideal for industrially scalable applications. 66

Here, we demonstrate the use of dewetted metal nanocaps  
67 on transparent silica surfaces to produce and customize  
68 structural colors. In particular, we demonstrate for the first  
69 time that by changing the contact angle of the nanocaps we can  
70 obtain larger tuning and narrower LSPRs than traditional 71

**Received:** February 10, 2016

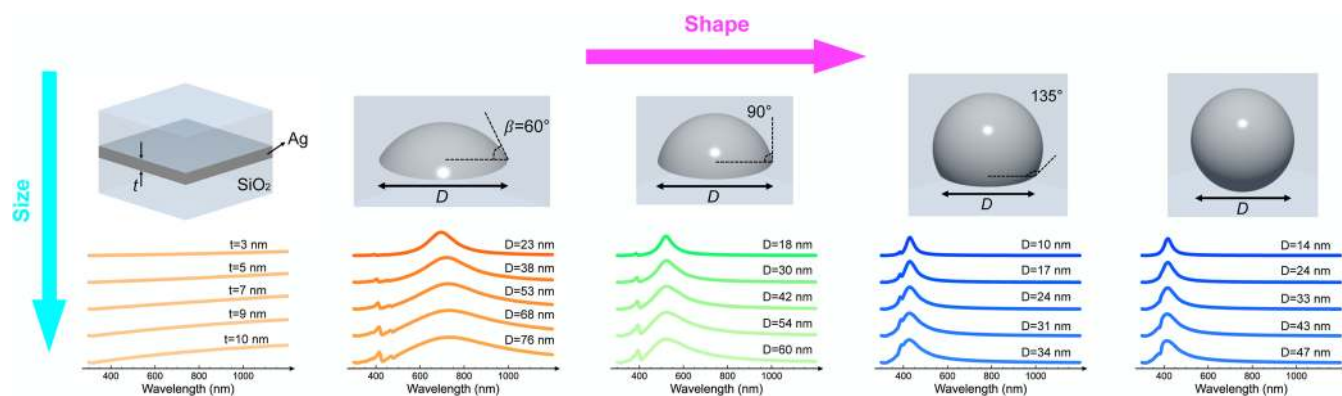


**Figure 1.** Color tuning through particle size and shape. Top: Geometry and parameters of a silver ultrathin metal film (UTMF) of thickness  $t$ , along with nanocaps of various shapes and sizes (base diameter  $D$  and contact angle  $\beta$ ), produced upon dewetting of the film. The metal is embedded in silica. We assume the nanocaps to be distributed in a triangular lattice with spacing  $8t$  and total metal volume equal to that of the homogeneous UTMF in all cases. Bottom: Calculated normal-incidence reflection spectra for particles of varying shape (horizontal direction) and size (vertical). Each curve is given the RGB color extracted from the spectrum that it represents.

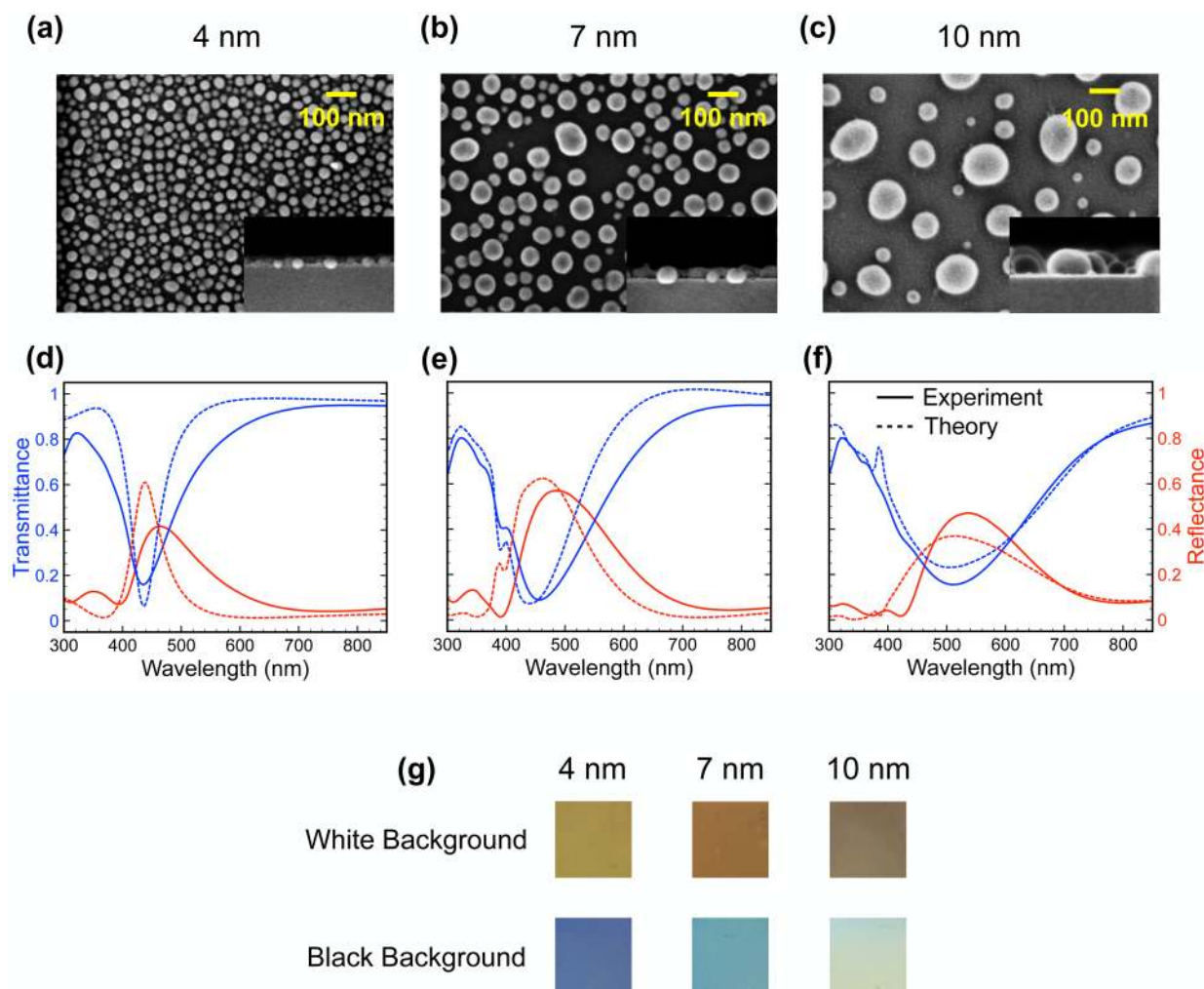


**Figure 2.** Color tuning through UTMF dewetting. We illustrate this concept with three representative samples produced upon dewetting of silver UTMFs. (a–c) Sample SEM images for different initial silver UTMF thicknesses (i.e., before dewetting; see top labels and also Table 1). (d–f) Measured (solid curves) and calculated (broken curves) normal-incidence transmission (blue curves) and reflection (red curves) spectra for the samples shown in (a)–(c). (g) Photographs for the three samples with measured spectra corresponding to (d)–(f) on white and black backgrounds.

72 approaches, for example, relying on changing particle size. A  
73 wide chromatic range is also accessible through varying the  
74 initial film thickness. The structures display a high degree of

dichroism, with radically different colors on transmission and 75  
76 reflection. We mainly focus on silver-on-silica, for which the 76  
77 contact angle determines the nanocap morphology, although 77

78 the method can be generally applied to other combinations of  
79 metal film and dielectric substrate. We gain further flexibility in  
80 color range and spectral absorbance by creating interfering  
81 structures with the addition of another properly spaced UTMF.

## 82 ■ RESULTS AND DISCUSSION

83 The power of changing the contact angle of nanocaps and of a  
84 straightforward dewetting process for structural coloring is  
85 clearly illustrated by Figure 1, which shows simulated reflection  
86 spectra of uniform and dewetted silver UTMFs embedded in  
87 silica for typical geometrical parameters similar to those of the  
88 actual samples (see below). When the UTMF thickness is  
89 increased in the  $t = 3\text{--}10$  nm range, the reflectance gradually  
90 grows at long wavelengths. This effect has a minor influence on  
91 reflection structural colors, which are mostly faded red (see  
92 Figure 1, in which different curves are given the RGB color  
93 computed from the spectra that they represent; see Materials  
94 and Methods for more details). However, a radical change in  
95 color is observed when moving from continuous UTMFs to  
96 dewetted nanocaps with different sizes and shapes (contact  
97 angle). As we show below, the average base diameter  $D$  and  
98 contact angle  $\beta$  can be controlled by the dewetting temperature,  
99 the duration of the thermal treatment used to induce dewetting,  
100 and the initial UTMF thickness; so these parameters allow us to  
101 generate on-demand bright structural colors, which are in all  
102 cases associated with the excitation of LSPRs in the nanocaps.  
103 In particular, we observe an excursion along a red-green-blue  
104 hue when the contact angle is varied in the  $\beta = 60\text{--}135^\circ$  range,  
105 driven by a change in plasmon resonance position. Generally,  
106 colors become lighter as the nanocap base diameter increases,  
107 due to LSPR broadening produced by radiative losses of the  
108 individual particles. For illustration, all reflection spectra of  
109 Figure 1 are calculated for triangular lattices of spacing  $8t$ , with  
110 nanocap size determined by the condition that the metal  
111 volume is maintained as in the initial film of thickness  $t$ , which  
112 results in the values of the base diameter  $D$  indicated by labels.  
113 Reflection spectra for spheres are also provided as a reference.  
114 Incidentally, we observe similar trends when examining arrays  
115 of particles with fixed base diameter but varying contact angle,  
116 in which the spacing is adjusted in order to maintain total metal  
117 volume as a constant (see Figure S1 in the Supporting  
118 Information (SI) for calculations of the transmittance as a  
119 function of light wavelength and incidence angle, indicating that  
120 LSPR-based coloring is robust against changes of incidence  
121 angle). In contrast to previous work, which focused on  
122 changing particle size (diameter), our proposed tuning scheme,  
123 relying on changing the contact angle, is much wider.  
124 Additionally, previous work has also shown that periodic  
125 structures can be used to achieve structural coloring, tuning the  
126 plasmonic response by changing the period.<sup>32–34</sup> However,  
127 such approaches suffer from either broad resonance  
128 features<sup>32,33</sup> or strong angular dependence of the obtained  
129 color.<sup>34</sup>  
130 We corroborate the potential of UTMF dewetting for  
131 coloring by preparing and optically characterizing samples  
132 consisting of silver on silica with different metal thicknesses  
133 (see Materials and Methods for fabrication details). A nearly  
134 index-matching 150 nm thick layer of poly(methyl methacry-  
135 late) (PMMA) is deposited on top (2% difference with the  
136 refractive index of the silica substrate; similar results are  
137 obtained with silica embedding; see Figure S2 in the SI). The  
138 results are summarized in Figure 2. In particular, Figure 2a–c  
139 shows SEM images of three samples, which produce the

transmission and reflection spectra plotted in Figure 2d–f, and  
these in turn generate the colors shown in Figure 2g.

As a rule, a larger initial metal thickness gives rise to lower  
particle density and larger particle size (Figure 2a–c). This  
increase in size switches on retardation, which in turn produces  
plasmon broadenings and red-shifts (Figure 2d–f). Similar  
conclusions can be extracted from samples of nanocaps exposed  
to air (see Figure S2 in the SI), but now the LSPRs are blue-  
shifted with respect to those covered with PMMA. The  
dielectric protection also prevents silver oxidation: we have  
verified their stable optical properties over a period of several  
months.

Figure 2g displays photographs taken from these three  
samples (Figure 2d–f). A large contrast in structural colors  
depending on whether the samples are on white or black  
background is evident.

We seek further understanding of our measurements (Figure  
2d–f, solid curves) by formulating an analytical theoretical  
model (broken curves), which is in excellent agreement with  
experiment in the details of the reflection/transmission spectra  
(Figure 2d–f). The model uses as input the geometrical  
parameters retrieved upon inspection of the sample SEM  
images (Figure 2a–c), which are summarized in Table 1. We

**Table 1. Statistical Parameters for Three Fabricated Samples with Different Initial Silver UTMF Thicknesses, as Extracted by SEM Image Analysis<sup>a</sup>**

initial film thickness (nm)	particle density ( $\mu\text{m}^{-2}$ )	average base diameter (nm)	diameter std (nm)	average height (nm)	estimated contact angle (deg)
4	805	20	9	16	116
7	210	34	14	35	128
10	35	82	30	71	120

<sup>a</sup>See Figure 2a–c. The contact angle is estimated from the height and base diameter assuming spherical nanocap profiles.

describe the particles as spherical nanocaps similar to those of  
Figure 1 and assume a fixed value of the silver-on-silica contact  
angle  $\beta = 120^\circ$ . The optical response of the nanocaps is  
reduced to their average anisotropic polarizability (for axial and  
transversal directions), which we combine with the dynamical  
interaction between them, taking into account their random  
distribution, to produce reflection and transmission coefficients  
(see Materials and Methods for more details). This model  
produces satisfactory results compared with experiment (Figure  
2d–f), except for the discrepancy in plasmon width of the  
thinner sample (Figure 2d), where the particle details are at the  
limit of the SEM spatial resolution, which probably affects the  
determination of statistic geometrical parameters.

The optical response of our samples emerges from the  
properties of the individual nanocaps and their LSPRs, which  
we investigate in more detail in Figure 3. In particular, the  
dependence on contact angle  $\beta$  is summarized in Figure 3a–c  
for small nanocaps (base diameter  $D = 10$  nm), for which  
retardation can be neglected. The response in the spectral range  
under consideration is dominated by the lowest order axial and  
transversal dipolar plasmons, whose spectral position and  
weight are fully captured by two parameters in the electrostatic  
limit, which we extract from boundary-element method  
electromagnetic simulations<sup>25</sup> (BEM; see methods): the value  
of the metal permittivity at which the plasmon shows up  
(Figure 3a) and the dipolar transition strength (Figure 3b). The



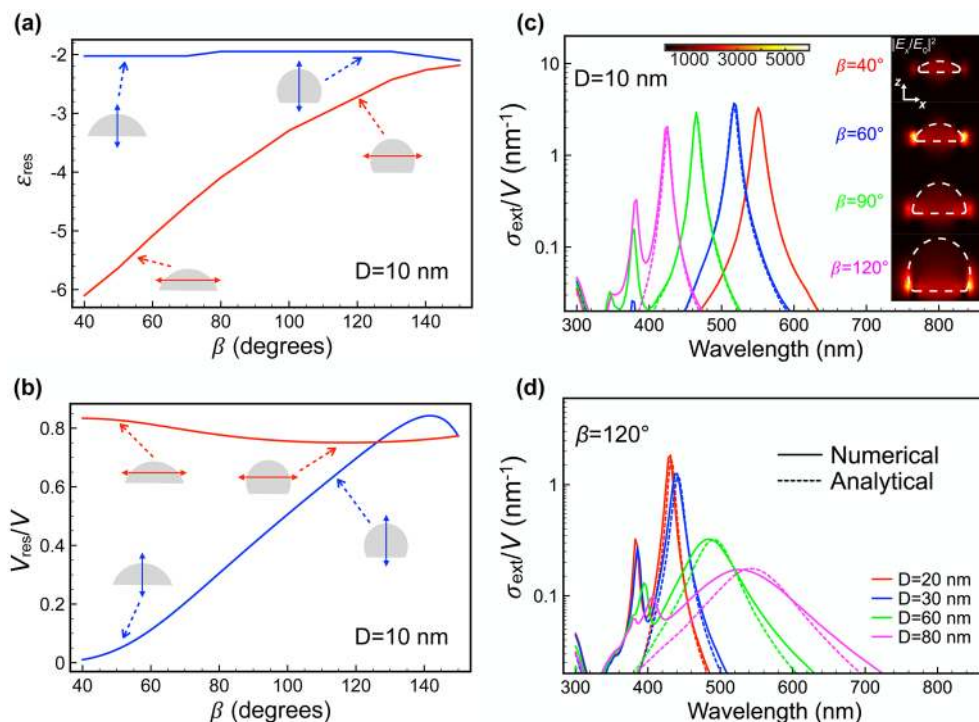


**Figure 3.** Plasmons in spherical nanocaps. (a) Resonant value of the permittivity for which a dipolar plasmon is sustained by nanocaps of varying shape (i.e., as a function of contact angle  $\beta$ ). Both transversal and axial polarizations are considered (see insets and double arrows). (b) Fractional contribution to the spectral weight for the plasmons considered in (a). (c) Normalized extinction spectra for light incident along the axial direction. Numerical electromagnetic simulations (solid curves) are well reproduced by a simple analytical model (dashed curves; see [Materials and Methods](#)) based on the dominant transversal plasmon. (d) Same as (c) for nanocaps of fixed shape ( $\beta = 120^\circ$ ) and different larger sizes (the legend indicates the base diameter  $D$ ), illustrating the ability of our model to cope with retardation effects (see [Materials and Methods](#)).

189 latter is expressed in terms of a fractional volume associated  
 190 with the resonance, and it amounts to the fraction that it  
 191 contributes to the integral of the extinction cross-section over  
 192 frequency. These two parameters are all the input that we need  
 193 to analytically describe the polarizability of the particles (see  
 194 [Materials and Methods](#)), from which we calculate the cross-  
 195 section represented in [Figure 3c](#) (broken curves). Despite the  
 196 simplicity of this method, we find a remarkable agreement of  
 197 the spectra with BEM simulations (broken curves). Notice that  
 198 under light incidence along the particle axis the transversal  
 199 plasmon dominates the response. Near-field plots associated  
 200 with this mode reveal light confinement and enhancement near  
 201 the edge of the particle base (see insets to [Figure 3c](#)). Unlike  
 202 the axial plasmon, the transversal one has a strong dependence  
 203 on contact angle ([Figure 3a](#)), whereas its spectral weight  
 204 remains at a high level of  $\sim 0.8$  ([Figure 3b](#)). This explains the  
 205 weak dependence of the optical properties of our samples on  
 206 incidence angle. Nevertheless, the axial plasmon can also be  
 207 excited in our nanostructures at larger incidence angle,  
 208 emerging as a feature at shorter wavelength (see [Figure S1](#) in  
 209 the [SI](#)).

210 When the particle size increases, retardation effects become  
 211 important, leading to plasmon red-shifting and broadening.  
 212 Both of these effects can be easily accounted for in a modified  
 213 analytical polarizability that we present in [Materials and](#)  
 214 [Methods](#). The results are in excellent agreement with  
 215 electromagnetic BEM simulations, as illustrated in [Figure 3d](#)  
 216 for nanocaps of shape and sizes similar to those involved in  
 217 the measured samples of [Figure 2](#). Additionally, the dominant  
 218 plasmon feature in the spectra is expected to blue-shift with

219 increasing contact angle (see [Figure 3c](#)), as the particle aspect  
 220 ratio is reduced. This result is fully corroborated by  
 221 measurements on additional samples in which a treatment of  
 222 the surface can produce a change in contact angle (see [Figure](#)  
 223 [S3](#) in the [SI](#)). Further comparisons between numerical and  
 224 theoretical results for nanocaps with other contact angles are  
 225 offered in [Figure S4](#) of the [SI](#).

226 Optical interference can also produce structural colors,  
 227 adding an extra knob to further tune the chromatic suite  
 228 achieved through metal dewetting. We test this principle by  
 229 adding an extra nickel layer of thickness varied from  $d = 3$  nm  
 230 (transparent) to 40 nm (opaque). In particular, we show in  
 231 [Figure 4a](#) results for samples produced by this procedure  
 232 starting with a dewetted 7 nm silver film, covered with 150 nm  
 233 of PMMA. A clear asymmetric plasmonic coloring effect is  
 234 observed in measurements from the two sides of the sample  
 235 (*front* and *back*, see scheme in [Figure 4a](#)). Transmittance from  
 236 both sides is identical in virtue of reciprocity, as corroborated in  
 237 both measurements and simulations (see [Figure 4b](#) and also  
 238 [Figure S5](#) in the [SI](#)), and it eventually evolves toward negligible  
 239 values as the nickel eventually becomes optically thick. In  
 240 contrast, there are clear differences in absorbance from both  
 241 sides: front-side absorption increases with nickel thickness  $d$  in  
 242 the 300–550 nm wavelength range, reaching values above 85%,  
 243 essentially as a result of a Salisbury screen effect;<sup>35</sup> however,  
 244 back-side absorption decreases with increasing  $d$ , attenuating  
 245 the effect of the dewetted silver layer and eventually saturating  
 246 at the bulk nickel surface absorption level. The chromatic  
 247 variation produced upon nickel deposition is illustrated by  
 248 photographs in [Figure 4c](#). We note that both in the spectra and

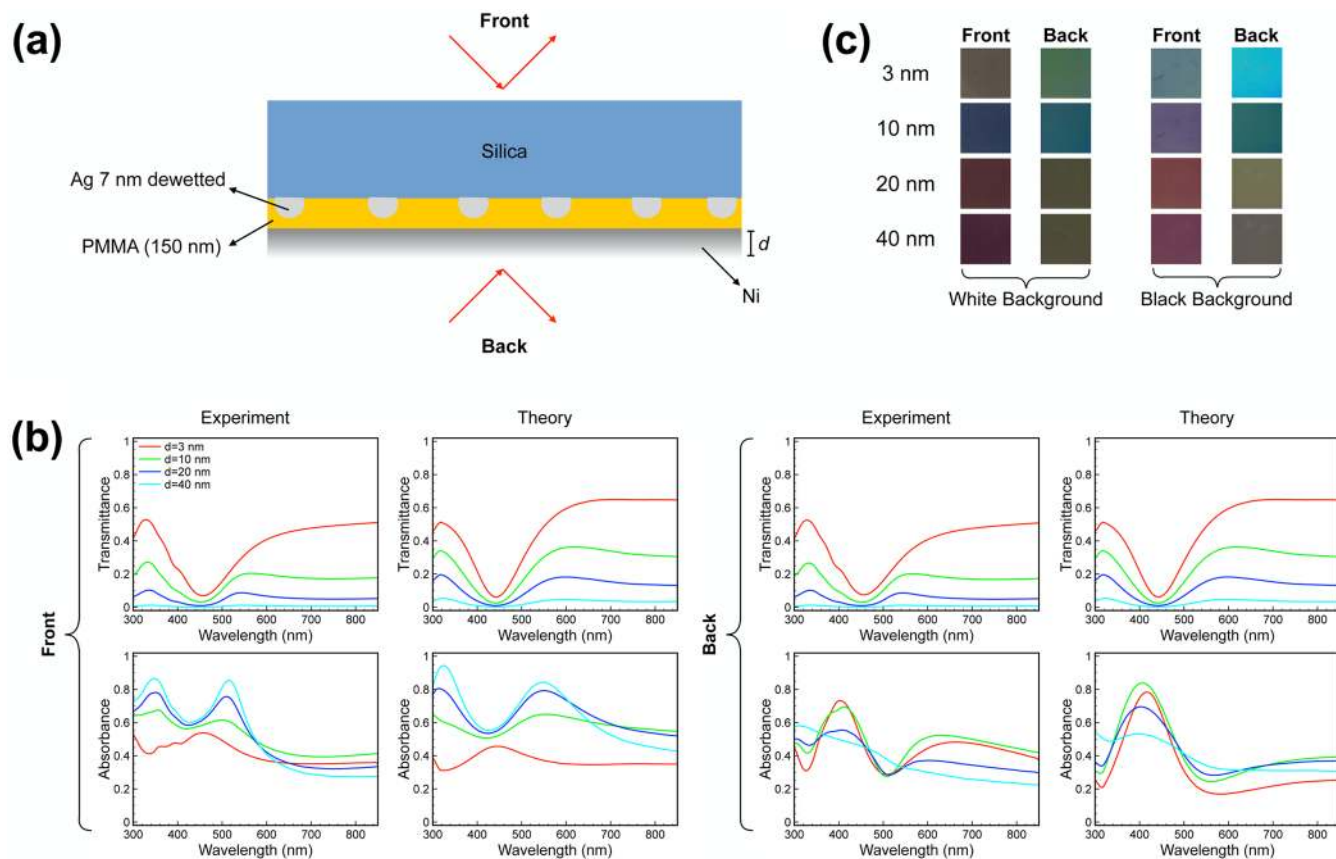


**Figure 4.** Additional color tuning through interference. (a) A nickel UTMF is deposited on a 150 nm PMMA spacer embedding the silver nanocaps that are previously obtained upon dewetting a 7 nm silver film. (b) Measured and calculated transmission and absorption spectra for normal-incidence illumination from the back and front sides of the structure (see (a)). We consider different nickel thicknesses in the  $d = 3\text{--}40$  nm range. (c) Photographs of the samples whose measured absorption (reflection) spectra are shown in (b), taken on white and black backgrounds.

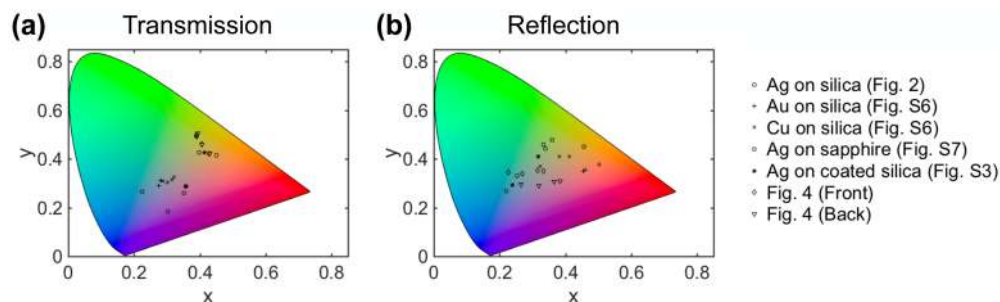


**Figure 5.** Position of the colors in our samples on the CIE 1931 map. We show the colors associated with our experimental spectra (see labels), as obtained for a D65 illumination light source.

249 in the resulting colors our simple theory compares reasonably  
250 well with experiment, including in this case the effect of  
251 multiple reflections at the different interfaces of the sample.

## 252 CONCLUSION

253 In summary, we have demonstrated that arrays of metal  
254 nanocaps created via a low-cost, lithography-free dewetting  
255 process display intense colors as a result of the excitation of  
256 localized surface plasmons in the particles. A wide chromatic  
257 range is accessible through careful control of the initial metal  
258 thickness and the dewetting conditions (temperature and  
259 duration), which ultimately defines the size, density, and  
260 contact angle of the resulting nanoparticles. Colors can be  
261 actually customized over a sizable range of the visible spectrum

for a wide range of incidence angles, as shown in Figure 5,  
where we represent the colors associated with our obtained  
experimental spectra superimposed on the Commission  
Internationale de l'Éclairage (CIE) 1931 color map. For  
example, we observe structures that go from reflective  
(scattered) red to green and blue, suggesting the potential for  
large-scale manufacturing of structurally colored glass windows,  
optical filters, and display panels.<sup>36</sup> The addition of an extra  
ultrathin metal film produces interference with the dewetted  
film, leading to further control over the chromatic properties.  
The combination of continuous and dewetted metal layers thus  
holds great potential to achieve full control over the visible  
spectral properties of thin films, which are accessible through  
industrially scalable, economic fabrication processes. Our

276 results can be readily extrapolated to other spectral regimes  
277 through a choice of appropriate materials (e.g., aluminum for  
278 the UV).

## 279 ■ MATERIALS AND METHODS

280 **Ultrathin Metal Film Deposition and Dewetting.** Silver  
281 ultrathin films are deposited on the silica substrate using a  
282 magnetron sputtering system (ATC Orion 8, AJA International,  
283 Inc. or KDF 903i). The coated substrates are then subjected to  
284 rapid thermal annealing in a Tsunami RTP-600S at a  
285 temperature of 750 °C for about 90 s under a nitrogen flow  
286 of 1 atm. In this way the ultrathin silver films are dewetted into  
287 nanocaps. The PMMA overlayer is deposited through spin-  
288 coating.

289 **Sample Characterization.** Optical transmittance and  
290 reflectance are measured using a UV–vis–NIR spectropho-  
291 tometer (PerkinElmer Lambda 950). The morphology of the  
292 nanocaps is examined with a field-emission scanning electron  
293 microscope (FEG-SEM, Inspect F, FEI Systems).

294 **Simulation of Individual Nanocaps.** The optical  
295 response of individual nanocaps is simulated using BEM.<sup>25</sup>  
296 The metal dielectric function is taken from tabulated data,<sup>26</sup>  
297 whereas a homogeneous surrounding medium is assumed with  
298 constant permittivity  $\epsilon_s = 2.13$  similar to that of silica and  
299 PMMA in the spectral region under investigation. The particle  
300 geometry is determined by its base diameter  $D$  and contact  
301 angle with the substrate  $\beta$ , while the edges are smoothed with a  
302 rounded radius of 0.5 nm. These simulations yield the particle  
303 extinction cross-section and its scattering matrix used to  
304 simulate arrays.

305 **Average Polarizability of Nanocaps in the Actual**  
306 **Samples.** For a given sample, the contact angle is roughly  
307 constant, and in particular, it takes the value  $\beta = 120^\circ$  for silver  
308 on silica. However, the particle size has a finite size distribution,  
309 which we describe through a Gaussian,

$$P(D) = \frac{1}{\sqrt{2\pi}\sigma} e^{-(D-\bar{D})^2/2\sigma^2}$$

310 as a function of the base diameter  $D$ , centered around its  
311 average  $\bar{D}$  with standard deviation  $\sigma$ . These parameters ( $\bar{D}$  and  
312  $\sigma$ ) depend on the initial UTMF thickness, as shown in Table 1.  
313 We then describe the particles through their average polar-  
314 ization:

$$\bar{\alpha}_{\parallel,\perp}(\omega) = -\frac{1}{k^2} \int f_{\parallel,\perp}(\omega, D) P(D) dD$$

315 where  $f_{\parallel,\perp}(\omega, D)$  is the far-field amplitude of individual  
316 nanocaps for transversal ( $\perp$ ) and axial ( $\parallel$ ) incident field  
317 polarization, calculated with BEM as noted above.

318 **Analytical Model for Individual Nanocaps.** We  
319 elaborate an analytical model based upon the dipolar response  
320 of the particles, supplemented to incorporate retardation  
321 effects, which are important for large sizes, although the  
322 particle diameters under consideration are still small compared  
323 with the wavelength, so that the dipolar response becomes  
324 dominant. In the electrostatic limit, the particle polarizability  
325 can be written as<sup>27</sup>

$$\alpha_{\text{es}}(\omega) = \frac{1}{4\pi\epsilon_s} \sum_j V_j \left[ \frac{1}{\epsilon(\omega) - \epsilon_s} - \frac{1}{\epsilon_s(\epsilon_j - 1)} \right]^{-1}$$

where  $\epsilon(\omega)$  and  $\epsilon_s$  are the permittivities of the metal in the  
particle and the dielectric host, respectively. Here, the sum  
extends over the electrostatic eigenmodes of the system, which  
are identified by eigenvalues  $\epsilon_j$  and contribute to the  
polarizability with a partial volume  $V_j$  (the sum of  $V_j$ 's is  
equal to the particle volume). Retardation produces two effects:  
(1) radiative damping, which we incorporate through the well-  
known prescription<sup>28</sup>

$$\alpha(\omega) = \frac{1}{\alpha_{\text{es}}^{-1} - 2ik^3/3}$$

where  $k = \omega/c$ ; and (2) plasmon red-shifts, which we  
phenomenologically describe through the substitution

$$\epsilon_j \rightarrow \frac{\epsilon_j}{\cos(k\xi D)} + \left[ 1 - \frac{1}{\cos(k\xi D)} \right] \frac{1}{\epsilon_s}$$

where  $\xi$  is a scaling factor. Finally, we compare the extinction  
cross-section computed with BEM (see above) with the  
analytical cross-section  $4\pi k \text{Im}\{\alpha(\omega)\}$  in order to extract fitting  
parameters  $\epsilon_j$ ,  $V_j$ , and  $\xi$ , which depend only on the geometrical  
contact angle  $\beta$ , but not on material composition and  
frequency. In particular, we find  $\xi = 0.75$  for the contact  
angle  $\beta = 120^\circ$  of silver on silica. In practice, we retain only the  
lowest order dipolar mode for polarization directions either  
parallel to the nanocap base (transverse) or along its rotation  
axis (axial).

**Simulation of Periodic Nanocap Arrays.** We use the  
layer-KKR method<sup>29</sup> to simulate the response of periodic  
particle arrays (see Figure S1 in the SI). A rigorous solution of  
Maxwell's equations is then obtained by describing the particles  
through their scattering matrix (i.e., their multipolar response),  
as obtained with BEM (see above).

**Analytical Model for Disordered Nanocap Arrays.** We  
formulate an analytical model of the response of the samples by  
describing the nanocaps through the average polarizability  $\bar{\alpha}$   
(see above), following similar methods to those reported  
elsewhere.<sup>30,31</sup> In particular, the reflection and transmission  
coefficients for p-polarized light with angle of incidence  $\theta$   
reduce to

$$r = \frac{i2\pi k\rho}{\cos\theta} \left( \frac{-\cos^2\theta}{\bar{\alpha}_{\parallel}^{-1} - G_{\parallel}} + \frac{\sin^2\theta}{\bar{\alpha}_{\perp}^{-1} - G_{\perp}} \right)$$

$$t = 1 - r + \frac{i2\pi k\rho}{\cos\theta} \frac{2\sin^2\theta}{\bar{\alpha}_{\perp}^{-1} - G_{\perp}}$$

where  $\rho$  is the particle density, whereas  $G_{\parallel,\perp}$  are the dipole-  
dipole interaction lattice sums. The latter allows the expression

$$G_{\parallel,\perp} = \int \frac{d^2\mathbf{Q}}{(2\pi)^2} \left[ \frac{1}{\rho} S(\mathbf{Q} - \mathbf{k}_{\parallel}) - 1 \right] \mathcal{G}_{\parallel,\perp}(\mathbf{Q})$$

in terms of the momentum representation of the dipole-  
dipole interaction components  
 $\mathcal{G}_{\perp}(\mathbf{Q}) = 2\pi i k_z Q_x^2 / Q^2 + 2\pi i (k^2 / k_z) (1 - Q_x^2 / Q^2)$  and  
 $\mathcal{G}_{\parallel}(\mathbf{Q}) = 2\pi i Q^2 / k_z$ , where  $k_z = \sqrt{k^2 - Q^2}$ , as extracted for  
both interacting dipoles oriented either perpendicular or  
parallel to the surface normal, respectively. The lattice sums  
also depend on the surface projection of the incident light wave  
vector  $\mathbf{k}_{\parallel}$  and the structure factor  $S(\mathbf{Q}) = \sum_{\mathbf{R}} \exp(i\mathbf{Q}\cdot\mathbf{R})$ , where  
the sum runs over particle positions. More precisely, we have



368  $S(\mathbf{Q}) = (2\pi\rho)^2 \delta(\mathbf{Q}) + \rho$  for a completely disordered array and  
369  $S(\mathbf{Q}) = (2\pi\rho)^2 \sum_{\mathbf{g}} \delta(\mathbf{Q}-\mathbf{g})$  for a periodic one, where  $\mathbf{g}$  runs  
370 over reciprocal lattice vectors. Theory curves in Figures 2 and 4  
371 are obtained assuming random particle distributions.  
372 **RGB Color.** We show RGB colors in several figures, as  
373 extracted from measured and calculated spectra, assuming a  
374 flat-spectrum illumination. RGB parameters are obtained  
375 simply by projection on the spectra of the three pigments  
376 that define this color scheme.

## 377 ■ ASSOCIATED CONTENT

### 378 ● Supporting Information

379 The Supporting Information is available free of charge on the  
380 ACS Publications website at DOI: 10.1021/acspphoto-  
381 nics.6b00090.

382 Further simulations and experiments and, in particular,  
383 calculations of the transmittance of ordered and  
384 disordered planar particle arrays for fixed particle size  
385 and different contact angles (Figure S1); measured  
386 reflection and transmission spectra for silver nanocaps  
387 with different surrounding media (Figure S2) and  
388 contact angles (Figure S3 and Table S1); an extension  
389 of Figure 3d to cover more contact angles (Figure S4);  
390 the reflectance spectra corresponding to the samples of  
391 Figure 4b (Figure S5); and measured spectra for gold  
392 and copper on silica (Figure S6) and silver on sapphire  
393 (Figure S7) (PDF)

## 394 ■ AUTHOR INFORMATION

### 395 Corresponding Authors

396 \*E-mail: javier.garciadeabajo@icfo.es.

397 \*E-mail: valerio.pruneri@icfo.es.

### 398 Notes

399 The authors declare no competing financial interest.

## 400 ■ ACKNOWLEDGMENTS

401 This work has been supported in part by Spanish MINECO  
402 (MAT2014-59096-P and SEV2015-0522), Fundació Privada  
403 Cellex, the European Commission (Graphene Flagship  
404 CNECT-ICT-604391 and FP7-ICT-2013-613024-GRASP),  
405 AGAUR (2014 SGR 1400 and 1623), and the Fondo Europeo  
406 de Desarrollo Regional (FEDER, TEC2013-46168-R).

## 407 ■ REFERENCES

408 (1) Freestone, I.; Meeks, N.; Sax, M.; Higgitt, C. The Lycurgus Cup -  
409 A Roman nanotechnology. *Gold Bulletin* **2007**, *40*, 270–277.  
410 (2) Kinoshita, S.; Yoshioka, S.; Miyazaki, J. Physics of structural  
411 colors. *Rep. Prog. Phys.* **2008**, *71*, 076401.  
412 (3) Inoue, D.; Miura, A.; Nomura, T.; Fujikawa, H.; Sato, K.; Ikeda,  
413 N.; Tsuya, D.; Sugimoto, Y.; Koide, Y. Polarization independent visible  
414 color filter comprising an aluminum film with surface-plasmon  
415 enhanced transmission through a subwavelength array of holes. *Appl.*  
416 *Phys. Lett.* **2011**, *98*, 093113.  
417 (4) Lee, H.-S.; Yoon, Y.-T.; Lee, S.-s.; Kim, S.-H.; Lee, K.-D. Color  
418 filter based on a subwavelength patterned metal grating. *Opt. Express*  
419 **2007**, *15*, 15457–15463.  
420 (5) Roberts, A. S.; Pors, A.; Albrektsen, O.; Bozhevolnyi, S. I.  
421 Subwavelength plasmonic color printing protected for ambient use.  
422 *Nano Lett.* **2014**, *14*, 783–787.  
423 (6) Si, G.; Zhao, Y.; Lv, J.; Lu, M.; Wang, F.; Liu, H.; Xiang, N.;  
424 Huang, T. J.; Danner, A. J.; Teng, J.; Liu, Y. J. Reflective plasmonic  
425 color filters based on lithographically patterned silver nanorod arrays.  
426 *Nanoscale* **2013**, *5*, 6243–6248.

(7) Xu, T.; Wu, Y.-K.; Luo, X.; Guo, L. J. Plasmonic nanoresonators  
427 for high-resolution colour filtering and spectral imaging. *Nat. Commun.*  
428 **2010**, *1*, 59.  
429 (8) Kumar, K.; Duan, H.; Hegde, R. S.; Koh, S. C. W.; Wei, J. N.;  
430 Yang, J. K. W. Printing colour at the optical diffraction limit. *Nat.*  
431 *Nanotechnol.* **2012**, *7*, 557–561.  
432 (9) Cheng, F.; Gao, J.; Luk, T. S.; Yang, X. Structural color printing  
433 based on plasmonic metasurfaces of perfect light absorption. *Sci. Rep.*  
434 **2015**, *5*, 11045.  
435 (10) Li, Z.; Clark, A. W.; Cooper, J. M. Dual Color Plasmonic Pixels  
436 Create a Polarization Controlled Nano Color Palette. *ACS Nano* **2016**,  
437 *10*, 492–498.  
438 (11) Clark, A. W.; Cooper, J. M. Plasmon Shaping by using Protein  
439 Nanoarrays and Molecular Lithography to Engineer Structural Color.  
440 *Angew. Chem.* **2012**, *124*, 3622–3626.  
441 (12) Olson, J.; Manjavacas, A.; Liu, L.; Chang, W.-S.; Foerster, B.;  
442 King, N. S.; Knight, M. W.; Nordlander, P.; Halas, N. J.; Link, S. Vivid,  
443 full-color aluminum plasmonic pixels. *Proc. Natl. Acad. Sci. U. S. A.*  
444 **2014**, *111*, 14348–14353.  
445 (13) Clausen, J. S.; Højlund-Nielsen, E.; Christiansen, A. B.; Yazdi,  
446 S.; Grajower, M.; Taha, H.; Levy, U.; Kristensen, A.; Mortensen, N. A.  
447 Plasmonic metasurfaces for coloration of plastic consumer products.  
448 *Nano Lett.* **2014**, *14*, 4499–4504.  
449 (14) Macleod, H. A. *Thin-Film Optical Filters*; CRC Press, 2001.  
450 (15) Lichtman, J. W.; Conchello, J. A. Fluorescence microscopy. *Nat.*  
451 *Methods* **2005**, *2*, 910–919.  
452 (16) Sampson, J. B.; Florence, J. M. Projection display system for  
453 reflective light valves. U.S. Patent US6,113,239, 2000.  
454 (17) Li, Z.; Butun, S.; Aydin, K. Large-Area, Lithography-Free Super  
455 Absorbers and Color Filters at Visible Frequencies Using Ultrathin  
456 Metallic Films. *ACS Photonics* **2015**, *2*, 183–188.  
457 (18) Kats, M. A.; Blanchard, R.; Genevet, P.; Capasso, F. Nanometre  
458 optical coatings based on strong interference effects in highly  
459 absorbing media. *Nat. Mater.* **2013**, *12*, 20–24.  
460 (19) Nassau, K. *The Physics and Chemistry of Color: The Fifteen Causes*  
461 *of Color*; Wiley-VCH: New York, 2001.  
462 (20) Yan, M.; Dai, J.; Qiu, M. Lithography-free broadband visible  
463 light absorber based on a mono-layer of gold nanoparticles. *J. Opt.*  
464 **2014**, *16*, 025002.  
465 (21) Mazumder, P.; Jiang, Y.; Baker, D.; Carrilero, A.; Tulli, D.;  
466 Infante, D.; Hunt, A. T.; Pruneri, V. Superomniphobic, transparent,  
467 and antireflection surfaces based on hierarchical nanostructures. *Nano*  
468 *Lett.* **2014**, *14*, 4677–4681.  
469 (22) Tulli, D.; Hart, S. D.; Mazumder, P.; Carrilero, A.; Tian, L.;  
470 Koch, K. W.; Yongsunthorn, R.; Piech, G. A.; Pruneri, V. Monolithically  
471 Integrated Micro- and Nanostructured Glass Surface with Antiglare,  
472 Antireflection, and Superhydrophobic Properties. *ACS Appl. Mater.*  
473 *Interfaces* **2014**, *14*, 11198–11203.  
474 (23) Thompson, C. V. Solid-state dewetting of thin films. *Annu. Rev.*  
475 *Mater. Res.* **2012**, *42*, 399–434.  
476 (24) Infante, D.; Koch, K. W.; Mazumder, P.; Tian, L.; Carrilero, A.;  
477 Tulli, D.; Baker, D.; Pruneri, V. Durable, superhydrophobic,  
478 antireflection, and low haze glass surfaces using scalable metal  
479 dewetting nanostructuring. *Nano Res.* **2013**, *6*, 429–440.  
480 (25) García de Abajo, F. J.; Howie, A. Retarded field calculation of  
481 electron energy loss in inhomogeneous dielectrics. *Phys. Rev. B:*  
482 *Condens. Matter Mater. Phys.* **2002**, *65*, 115418.  
483 (26) Johnson, P. B.; Christy, R. W. Optical constants of the noble  
484 metals. *Phys. Rev. B* **1972**, *6*, 4370–4379.  
485 (27) Solís, D. M.; Taboada, J. M.; Obelleiro, F.; Liz-Marzán, L. M.;  
486 García de Abajo, F. J. Toward ultimate nanoplasmonics modeling. *ACS*  
487 *Nano* **2014**, *8*, 7559–7570.  
488 (28) Draine, B. T. The discrete-dipole approximation and its  
489 application to interstellar graphite grains. *Astrophys. J.* **1988**, *333*, 848–  
490 872.  
491 (29) Stefanou, N.; Yannopoulos, V.; Modinos, A. MULTEM 2: A new  
492 version of the program for transmission and band-structure  
493 calculations of photonic crystals. *Comput. Phys. Commun.* **2000**, *132*,  
494 189–196.  
495

- 496 (30) García de Abajo, F. J. Colloquium: Light scattering by particle  
497 and hole arrays. *Rev. Mod. Phys.* **2007**, *79*, 1267–1290.
- 498 (31) Stauber, G. G.; García de Abajo, F. J. Extraordinary absorption  
499 of decorated undoped graphene. *Phys. Rev. Lett.* **2014**, *112*, 077401.
- 500 (32) Shrestha, V. R.; Lee, S.-S.; Kim, E.-S.; Choi, D.-Y. Aluminum  
501 plasmonics based highly transmissive polarization-independent sub-  
502 tractive color filters exploiting a nanopatch array. *Nano Lett.* **2014**, *14*,  
503 6672–6678.
- 504 (33) Tan, S. J.; Zhang, L.; Zhu, D.; Goh, X. M.; Wang, Y. M.; Kumar,  
505 K.; Qiu, C.-W.; Yang, J. K. Plasmonic color palettes for photorealistic  
506 printing with aluminum nanostructures. *Nano Lett.* **2014**, *14*, 4023–  
507 4029.
- 508 (34) Shen, Y.; Rinnerbauer, V.; Wang, I.; Stelmakh, V.;  
509 Joannopoulos, J. D.; Soljacic, M. Structural colors from Fano  
510 resonances. *ACS Photonics* **2015**, *2*, 27–32.
- 511 (35) Munk, B. A. *Frequency Selective Surfaces: Theory and Design*; John  
512 Wiley & Sons, 2005.
- 513 (36) Hsu, C. W.; Zhen, B.; Qiu, W.; Shapira, O.; DeLacy, B. G.;  
514 Joannopoulos, J. D.; Soljačić, M. Transparent displays enabled by  
515 resonant nanoparticle scattering. *Nat. Commun.* **2014**, *5*, 3152.